

# Wideband Semiconductor Optical Amplifier Steady-State Numerical Model

Michael J. Connelly, *Member, IEEE*

**Abstract**—A wideband steady-state model and efficient numerical algorithm for a bulk InP–InGaAsP homogeneous buried ridge stripe semiconductor optical amplifier is described. The model is applicable over a wide range of operating regimes. The relationship between spontaneous emission and material gain is clarified. Simulations and comparisons with experiment are given which demonstrate the versatility of the model.

**Index Terms**—Modeling, semiconductor optical amplifier.

## I. INTRODUCTION

SEMICONDUCTOR optical amplifier (SOA) technology has matured to the point where commercial devices are available for use in optical communication systems. Mathematical models are required to aid in the design of SOAs and to predict their operational characteristics. Many such models have been presented in the literature [1]–[5]. However, many of these models make assumptions that restrict the range of operating conditions over which the SOA can be modeled. These assumptions are used either to obtain analytic solutions for the amplifier characteristics, or to aid numerical computation. SOAs can be used to simultaneously amplify a number of signals at different wavelengths. To model such an application, a wideband model of the SOA is required. In this paper, a comprehensive wideband model of a bulk InP–InGaAsP SOA is presented. Through the use of suitable gain models it can be extended to SOAs with quantum-well active regions. In the model, the relationship between spontaneous and stimulated emission is clarified. This relationship does not require the use of a spontaneous emission factor used in many models. Spontaneous emission within the amplifier is modeled by traveling-wave power equations, which neglect the phase of the spontaneous signal. The model can be applied to determine the steady-state properties of an SOA over a wide range of operating regimes. A numerical algorithm is described which enables efficient implementation of the model. Simulations and comparisons with experiment are given which demonstrate the versatility of the model.

## II. AMPLIFIER STRUCTURE AND BULK MATERIAL MODEL

The SOA modeled is a 1.55- $\mu\text{m}$  InP–In<sub>1-x</sub>Ga<sub>x</sub>As<sub>y</sub>P<sub>1-y</sub> homogeneous buried ridge stripe device with schematic cross-section shown in Fig. 1 [6].  $y$  and  $x$  are the molar fractions of Ar-

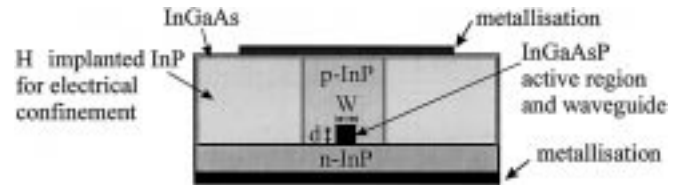


Fig. 1. Homogenous buried ridge stripe SOA schematic cross-section [6].

senide and Gallium, respectively, in the undoped active region. Lattice matching is assumed, for which  $x = 0.47y$ . The device structure consists of central active region of width  $W$ , thickness  $d$ , and length  $L_c$ . The active region narrows linearly as a lateral taper of width  $W$  at the central region to zero width at each end. Each taper has length  $L_t$ . The tapers reduce the optical confinement factor from its maximum value  $\Gamma$  at the central active region to zero at the amplifier ends. This causes the guided mode lateral profile to expand which improves the input and output coupling efficiencies to single mode optical fiber. As a first approximation the SOA is modeled as a device of mean length  $L$ , given by

$$L = L_c + L_t \quad (1)$$

with identical geometrical properties and an optical confinement factor as the central active region. Pertinent geometrical and material parameters for the device under consideration are given in Table I. The InGaAsP direct bandgap bulk-material active region has a material gain coefficient  $g_m(m^{-1})$  [7], given by

$$g_m(\nu, n) = \frac{c^2}{4\sqrt{2}\pi^{3/2}n_1^2\tau\nu^2} \left( \frac{2m_e m_{hh}}{\hbar(m_e + m_{hh})} \right)^{3/2} \times \int_0^\infty \left[ \sqrt{\nu' - \frac{E_g(n)}{h}} (f_c(\nu') - f_v(\nu')) \right] \times \left( \frac{2T_0}{(1 + (2\pi T_0)^2(\nu' - \nu)^2)} \right) d\nu' \quad (2)$$

where

$c$	speed of light in a vacuum;
$\nu$	optical frequency;
$n_1$	active region refractive index;
$\tau$	radiative carrier recombination lifetime [see (52)];
$\hbar$	Planck's constant $h$ divided by $2\pi$ ;
$m_e, m_{hh}$	conduction band (CB) electron and valence band (VB) heavy hole effective masses, respectively;
$n$	CB carrier (electron) density.
$T_0$	mean lifetime for coherent interaction of electrons with a monochromatic field and is of the order of 1 ps.

Manuscript received February 22, 2000; revised November 22, 2000. This work was supported in part by the European Union under the IST HARMONICS Project.

The author is with the Department of Electronic and Computer Engineering, University of Limerick, Limerick, Ireland (e-mail: michael.connelly@ul.ie).

Publisher Item Identifier S 0018-9197(01)01616-5.

TABLE I  
SOA GEOMETRICAL AND MATERIAL PARAMETERS

Symbol	Parameter	Value
$y$	Molar fraction of Arsenide in the active region	0.892 [6]
$L_c$	Central active region length	600 $\mu\text{m}$ [6]
$L_t$	Tapered active region length	100 $\mu\text{m}$ [6]
$d$	Active region thickness	0.4 $\mu\text{m}$ [6]
$W$	Central active region width	0.4 $\mu\text{m}$ [6]
$\Gamma$	Optical confinement factor	0.45 [6]
$K_g$	Bandgap shrinkage coefficient	$0.9 \times 10^{-10}$ eVm [9]
$n_1$	InGaAsP active region refractive index	3.22 [18]
$n_2$	InP region refractive index	3.167 [18]
$\frac{dn_1}{dn}$	Differential of active region refractive index with respect to carrier density	$-1.8 \times 10^{-26}$ m <sup>-3</sup> [18]
$n_{eq0}$	Equivalent refractive index at zero carrier density (from (29))	3.22
$\frac{dn_{eq}}{dn}$	Differential of equivalent refractive index with respect to carrier density (from (30))	$-1.34 \times 10^{-26}$ m <sup>-3</sup>
$\eta_{in}$	Input coupling loss	3.0 dB [6]
$\eta_{out}$	Output coupling loss	3.0 dB [6]
$R_1$	Input facet reflectivity	$5.0 \times 10^{-3}$ [6]
$R_2$	Output facet reflectivity	$5.0 \times 10^{-3}$ [6]
$K_o$	Carrier independent absorption loss coefficient	6200 m <sup>-1</sup>
$K_l$	Carrier dependent absorption loss coefficient	7500 m <sup>2</sup>
$A_{rad}$	Linear radiative recombination coefficient	$1.0 \times 10^{-7}$ s <sup>-1</sup>
$B_{rad}$	Bimolecular radiative recombination coefficient	$5.6 \times 10^{-16}$ m <sup>3</sup> s <sup>-1</sup>
$A_{nrad}$	Linear nonradiative recombination coefficient due to traps	$3.5 \times 10^8$ s <sup>-1</sup>
$B_{nrad}$	Bimolecular nonradiative recombination coefficient	$0.0 \times 10^{-16}$ m <sup>3</sup> s <sup>-1</sup>
$C_{aug}$	Auger recombination coefficient	$3.0 \times 10^{-41}$ m <sup>6</sup> s <sup>-1</sup>
$D_{leak}$	Leakage recombination coefficient	$0.0 \times 10^{48}$ m <sup>13.5</sup> s <sup>-1</sup>
$a$	Bandgap energy quadratic coefficient	1.35 [8]
$b$	Bandgap energy quadratic coefficient	-0.775 [8]
$c$	Bandgap energy quadratic coefficient	0.149 [8]
$m_e$	Effective mass of electron in the CB	$4.10 \times 10^{-32}$ kg [18]
$m_{hh}$	Effective mass of a heavy hole in the VB	$4.19 \times 10^{-31}$ kg [18]
$m_{hl}$	Effective mass of a light hole in the VB	$5.06 \times 10^{-32}$ kg [18]

The bandgap energy  $E_g$  can be expressed as

$$E_g(n) = E_{g0} - \Delta E_g(n). \quad (3)$$

$E_{g0}$ , the bandgap energy with no injected carriers, is given by the quadratic approximation [8]

$$E_{g0} = e(a + by + cy^2) \quad (4)$$

where  $a, b$  and  $c$  are the quadratic coefficients and  $e$  the electronic charge.  $\Delta E_g(n)$  is the bandgap shrinkage due to the injected carrier density [9] given by

$$\Delta E_g(n) = eK_g n^{1/3} \quad (5)$$

where  $K_g$  is the bandgap shrinkage coefficient. The value of  $K_g$  used in the model is taken to be slightly less than the value for In<sub>0.15</sub>Ga<sub>0.85</sub>As. The main effect of  $\Delta E_g$  is to shift the peak of

the gain and spontaneous emission spectra toward longer wavelengths.

The Fermi-Dirac distributions in the CB and VB [7] are given by

$$f_c(\nu) = \left\{ \exp\left(\frac{E_a - E_{fc}}{kT}\right) + 1 \right\}^{-1} \quad (6)$$

$$f_v(\nu) = \left\{ \exp\left(\frac{E_b - E_{fv}}{kT}\right) + 1 \right\}^{-1} \quad (7)$$

where

$$E_a = (h\nu - E_g(n)) \frac{m_{lh}}{m_e + m_{lh}}$$

$$E_b = -(h\nu - E_g(n)) \frac{m_e}{m_e + m_{lh}}. \quad (8)$$

$T$  is absolute temperature and  $k$  the Boltzmann constant.  $E_{fc}$  is the quasi-Fermi level of the CB relative to the bottom of the band.  $E_{fv}$  is the quasi-Fermi level of the VB relative to the top

of the band. They can be estimated using the Nilsson approximation [10]

$$\begin{aligned} E_{fc} &= \{\ln \delta + \delta[64 + 0.05524\delta(64 + \sqrt{\delta})]^{-\frac{1}{4}}\}kT \\ E_{fv} &= -\{\ln \varepsilon + \varepsilon[64 + 0.05524\varepsilon(64 + \sqrt{\varepsilon})]^{-\frac{1}{4}}\}kT \end{aligned} \quad (9)$$

where

$$\delta = \frac{n}{n_c}; \quad \varepsilon = \frac{p}{n_v}. \quad (10)$$

$p$  is the VB hole density. At the carrier density levels usually present in SOAs,  $p$  is equal to  $n$ .  $n_c$  and  $n_v$  are constants given by

$$n_c = 2 \left( \frac{m_e kT}{2\pi \hbar^2} \right)^{\frac{3}{2}}; \quad n_v = 2 \left( \frac{m_{lh} kT}{2\pi \hbar^2} \right)^{\frac{3}{2}} \quad (11)$$

where

$$m_{lh} = \left( m_{lh}^{\frac{3}{2}} + m_{lh}^{\frac{3}{2}} \right)^{\frac{2}{3}}. \quad (12)$$

$m_{lh}$  is the effective mass of a light hole in the VB. In (2), we can make the substitution

$$\left( \frac{2T_0}{(1 + (2\pi T_0)^2(\nu' - \nu)^2)} \right) = \delta(\nu - \nu') \quad (13)$$

as this function has a much narrower spectrum than the other terms within the integral [7]. Hence, (2) becomes

$$\begin{aligned} g_m(\nu, n) &= \frac{c^2}{4\sqrt{2}\pi^{3/2}n_1^2\tau\nu^2} \left( \frac{2m_em_{lh}}{\hbar(m_e + m_{lh})} \right)^{3/2} \\ &\times \sqrt{\nu - \frac{E_g(n)}{h}} (f_c(\nu) - f_v(\nu)). \end{aligned} \quad (14)$$

$g_m$  is composed of two components, a gain coefficient  $g'_m (\geq 0)$  and an absorption coefficient  $g''_m (\geq 0)$ , so

$$g_m = g'_m - g''_m \quad (15)$$

where

$$\begin{aligned} g'_m &= \frac{c^2}{4\sqrt{2}\pi^{3/2}n_1^2\tau\nu^2} \left( \frac{2m_em_{lh}}{\hbar(m_e + m_{lh})} \right)^{3/2} \\ &\times \sqrt{\nu - \frac{E_g(n)}{h}} f_c(\nu)(1 - f_v(\nu)) \end{aligned} \quad (16)$$

$$\begin{aligned} g''_m &= \frac{c^2}{4\sqrt{2}\pi^{3/2}n_1^2\tau\nu^2} \left( \frac{2m_em_{lh}}{\hbar(m_e + m_{lh})} \right)^{3/2} \\ &\times \sqrt{\nu - \frac{E_g(n)}{h}} (1 - f_c(\nu))f_v(\nu). \end{aligned} \quad (17)$$

Typical spectral plots of  $g_m$  and  $g'_m$  are shown in Fig. 2. To enable fast computations, the net gain coefficient is often approximated by a polynomial that is a function of the photon wavelength and carrier density. However, such approximations are

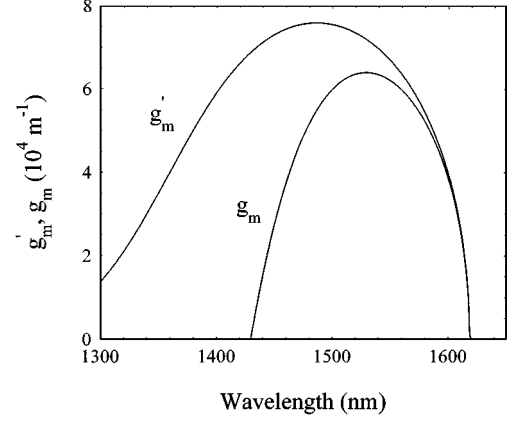


Fig. 2. Typical InGaAsP bulk semiconductor  $g_m$  and  $g'_m$  spectra. The carrier density is  $2.0 \times 10^{24} \text{ m}^{-3}$ .

usually only valid for wavelengths near the gain peak. The material loss coefficient  $\alpha (\text{m}^{-1})$  is modeled as a linear function of carrier density [11]

$$\alpha(n) = K_0 + \Gamma K_1 n. \quad (18)$$

$K_0$  and  $K_1$  are the carrier-independent and carrier-dependent absorption loss coefficients, respectively.  $K_0$  represents the intrinsic material loss.  $K_1$  is mainly due to intervalence band absorption.

### III. TRAVELING-WAVE EQUATIONS FOR THE SIGNAL FIELDS

In the model,  $N_s$  signals are injected with optical frequencies  $\nu_k$  ( $k = 1$  to  $N_s$ ) and power  $P_{\text{in}k}$  before coupling loss. The signals travel through the amplifier, aided by the embedded waveguide, and exit at the opposite facet. The SOA model is based on a set of coupled differential equations that describe the interaction between the internal variables of the amplifier, i.e., the carrier density and photon rates. The solution of these equations enables external parameters such as signal fiber-to-fiber gain and mean noise output to be predicted. In the following analysis, it is assumed that transverse variations in the photon rates and carrier density are negligible. This assumption is valid for SOAs with narrow active regions. In the model, the left (input) and right (output) facets have power reflectivities  $R_1$  and  $R_2$ , respectively. Within the amplifier, the spatially varying component of the field due to each input signal can be decomposed into two complex traveling-waves,  $E_{s_k}^+$  and  $E_{s_k}^-$ , propagating in the positive and negative  $z$  directions, respectively.  $z$  lies along the amplifier axis with its origin at the input facet. The modulus squared of the amplitude of a traveling-wave is equal to the photon rate ( $\text{s}^{-1}$ ) of the wave in that direction, so

$$N_{s_k}^+ = |E_{s_k}^+|^2; \quad N_{s_k}^- = |E_{s_k}^-|^2. \quad (19)$$

The lightwave representing the signal must be treated coherently since its transmission through the amplifier depends on its frequency and phase when reflecting facets are present.  $E_{s_k}^+$  and  $E_{s_k}^-$  obey the complex traveling-wave equations [2]

$$\frac{dE_{s_k}^+(z)}{dz} = \left( -j\beta_k + \frac{1}{2}(\Gamma g_m(\nu_k, n) - \alpha(n)) \right) E_{s_k}^+(z) \quad (20)$$

$$\frac{dE_{s_k}^-(z)}{dz} = \left( j\beta_k - \frac{1}{2}(\Gamma g_m(\nu_k, n) - \alpha(n)) \right) E_{s_k}^-(z) \quad (21)$$

where  $j = \sqrt{-1}$ . (20) and (21) are subject to boundary conditions

$$\begin{aligned} E_{s_k}^+(0) &= (1 - r_1)E_{\text{in}_k} + r_1 E_{s_k}^-(0) \\ E_{s_k}^-(L) &= r_2 E_{s_k}^+(L) \end{aligned} \quad (22)$$

where the  $k$ -th input signal field to the left of the input facet is

$$E_{\text{in}_k} = \sqrt{\frac{\eta_{\text{in}} P_{\text{in}_k}}{h\nu_k}}. \quad (23)$$

The  $k$ -th output signal field to the right of the output facet is

$$E_{\text{out}_k} = (1 - r_2)E_{s_k}^+(L). \quad (24)$$

The  $k$ -th output signal power after coupling loss is

$$P_{\text{out}_k} = h\nu_k \eta_{\text{out}} |E_{\text{out}_k}|^2. \quad (25)$$

$\eta_{\text{in}}$  and  $\eta_{\text{out}}$  are the input and output coupling efficiencies, respectively. The amplitude reflectivity coefficients are

$$r_1 = \sqrt{R_1}; \quad r_2 = \sqrt{R_2}. \quad (26)$$

The  $k$ -th signal propagation coefficient is

$$\beta_k = \frac{2\pi n_{\text{eq}} \nu_k}{c}. \quad (27)$$

$n_{\text{eq}}$  is the equivalent index of the amplifier waveguide [11] given by

$$n_{\text{eq}} = \left[ (n_1^2 - n_2^2) \frac{\Gamma}{2 - \Gamma} + n_2^2 \right]^{1/2}. \quad (28)$$

$n_2$  is the refractive index of the InP material surrounding the active region.  $n_{\text{eq}}$  is modeled as a linear function of carrier density [19]

$$n_{\text{eq}} = n_{\text{eq}0} + \frac{dn_{\text{eq}}}{dn} n. \quad (29)$$

$n_{\text{eq}0}$  is the equivalent refractive index with no pumping. The differential in (29) is given by

$$\frac{dn_{\text{eq}}}{dn} = \frac{n_1 \Gamma}{n_{\text{eq}0}(2 - \Gamma)} \frac{dn_1}{dn}. \quad (30)$$

Numerical values for  $n_{\text{eq}0}$  and  $dn_{\text{eq}}/dn$  are given in Table I.

#### IV. TRAVELING-WAVE EQUATIONS FOR THE SPONTANEOUS EMISSION

The amplification of the signal also depends on the amount of spontaneously emitted noise generated by the amplifier. This is because the noise power takes part in draining the available carrier population and helps saturate the gain. However, it is not necessary to treat the spontaneous emission as a coherent signal, since it distributes itself continuously over a relatively wide band of wavelengths with random phases between adjacent

wavelength components. When reflecting facets are present, the spontaneously emitted noise will show the presence of longitudinal cavity modes. For this reason, it may be assumed that noise photons only exist at discrete frequencies corresponding to integer multiples of cavity resonances. These frequencies are given by

$$\nu_j = \nu_c + \Delta\nu_c + jK_m \Delta\nu_m, \quad j = 0 \dots N_m - 1 \quad (31)$$

where the cutoff frequency at zero injected carrier density is given by

$$\nu_c = \frac{E_{g0}}{h}. \quad (32)$$

$\Delta\nu_c$  is a frequency offset used to match  $\nu_0$  to a resonance.  $K_m$  and  $N_m$  are positive integers. The values of  $K_m$  and  $N_m$  chosen depend on the gain bandwidth of the SOA and accuracy required from the numerical solution of the model equations. The longitudinal mode frequency spacing is

$$\Delta\nu_m = \frac{c}{2 \int_0^L n_{\text{eq}} dz}. \quad (33)$$

This technique can be applied to both resonant and near-traveling-wave SOAs and greatly reduces computation time. The detailed shape of the noise output can then be determined using the method shown in Section VII. It can be shown that averaging the coherent signal over two adjacent cavity resonances is identical to treating the signal coherently in terms of traveling-wave power (or photon rate) equations. It is sufficient to describe the spontaneous emission in terms of power, while signals must be treated in terms of waves with definite amplitude and phase.  $N_j^+$  and  $N_j^-$  are defined as the spontaneous emission photon rates ( $\text{s}^{-1}$ ) for a particular polarization [transverse electric (TE) or transverse magnetic (TM)] in a frequency spacing  $K_m \Delta\nu_m$  centered on frequency  $\nu_j$ , traveling in the positive and negative  $z$  directions, respectively.  $N_j^+$  and  $N_j^-$  obey the traveling-wave equations

$$\frac{dN_j^+(z)}{dz} = (\Gamma g_m(\nu_j, n) - \alpha(n))N_j^+ + R_{\text{sp}}(\nu_j, n) \quad (34)$$

$$\frac{dN_j^-(z)}{dz} = -(\Gamma g_m(\nu_j, n) - \alpha(n))N_j^- + R_{\text{sp}}(\nu_j, n) \quad (35)$$

subject to the boundary conditions

$$N_j^+(0) = R_1 N_j^-(0), \quad N_j^-(L) = R_2 N_j^+(L). \quad (36)$$

The function  $R_{\text{sp}}(\nu_j, n)$  represents the spontaneously emitted noise coupled into  $N_j^+$  or  $N_j^-$ . An expression for  $R_{\text{sp}}$  can be derived by a comparison between the noise output from an ideal amplifier obtained using (34) with the quantum mechanically derived expression [12]. An ideal amplifier has no gain saturation (which implies a constant carrier density throughout the amplifier), material gain coefficient  $g_m = g'_m(>0)$ , and zero loss coefficient, facet reflectivities, and coupling losses. In this case,  $N_j^+$  is obtained from the solution to

$$\frac{dN_j^+}{dz} = \Gamma g'_m(\nu_j, n) N_j^+ + R_{\text{sp}}(\nu_j, n). \quad (37)$$

The solution of (37), in this ideal case, gives an output noise power at a single polarization in a frequency band  $K_m\Delta\nu_m$  centered on  $\nu_j$  of

$$N_{\text{out}} = \frac{G-1}{\Gamma g'_m(\nu_j, n)} h\nu_j R_{\text{sp}}(\nu_j, n) \quad (38)$$

where  $G$  is the amplifier gain at  $\nu_j$ . The equivalent quantum mechanical expression [7] is

$$N_{\text{out}} = (G-1)h\nu_j K_m \Delta\nu_m. \quad (39)$$

Equating (38) with (39) gives

$$R_{\text{sp}}(\nu_j, n) = \Gamma g'_m(\nu_j, n) K_m \Delta\nu_m. \quad (40)$$

The traveling-wave power equations describing  $N_j^+$  and  $N_j^-$  assume that all the spontaneous photons in spacing  $K_m\Delta\nu_m$  are at resonance frequencies. In a real device the injected spontaneous photons, originating from  $R_{\text{sp}}$ , are uniformly spread over  $K_m\Delta\nu_m$ . The noise is filtered by the amplifier cavity. To account for this,  $N_j^+$  and  $N_j^-$  are multiplied by a normalization factor  $K_j$  which is derived as follows. If the single-pass gain is  $G_s$  at  $\nu_j$ , then the signal gain for frequencies within spacing  $\Delta\nu_m$  around  $\nu_j$  [2] is

$$G(\nu) = \frac{(1-R_1)(1-R_2)G_s}{(1-\sqrt{R_1 R_2} G_s)^2 + 4G_s \sqrt{R_1 R_2} \sin^2 \phi} \quad (41)$$

where the single-pass phase shift is

$$\phi = \frac{2\pi\nu}{c} \int_0^L n_{\text{eq}}(z) dz. \quad (42)$$

At resonance, the signal gain is

$$G(\nu_j) = \frac{(1-R_1)(1-R_2)G_s}{(1-\sqrt{R_1 R_2} G_s)^2}. \quad (43)$$

Let the amplifier have a noise input spectral density  $\sigma_{\text{in}}$  (photons/s/Hz) distributed uniformly over  $\Delta\nu_m$  centered at  $\nu_j$ . The total output noise (photons/s) in  $\Delta\nu_m$  is then

$$\begin{aligned} N_{\text{out}} &= \sigma_{\text{in}} \int_{\nu=\nu_j-\Delta\nu_m/2}^{\nu=\nu_j+\Delta\nu_m/2} G(\nu) d\nu \\ &= \sigma_{\text{in}} \Delta\nu_m \frac{1}{\pi} \int_0^\pi G(\phi) d\phi. \end{aligned} \quad (44)$$

If the input noise power were concentrated at  $\nu_j$  (resonance), then the output noise photon rate would be

$$N_{\text{resout}} = \sigma_{\text{in}} \Delta\nu_m G(\nu_j) K_j. \quad (45)$$

The factor  $K_j$  is included in (45) to equate  $N_{\text{out}}$  with  $N_{\text{resout}}$ , so

$$K_j = \frac{\int_0^\pi G(\phi) d\phi}{\pi G(\nu_j)} = \frac{1}{\pi} \int_0^\pi \frac{d\phi}{1 + \gamma^2 \sin^2(\phi)} \quad (46)$$

where

$$\gamma = \frac{4G_s(\nu_j)\sqrt{R_1 R_2}}{(1-\sqrt{R_1 R_2} G_s(\nu_j))^2}. \quad (47)$$

$K_j$  is equal to unity for zero facet reflectivities.

## V. CARRIER-DENSITY RATE EQUATION

The carrier density at  $z$  obeys the rate equation

$$\begin{aligned} \frac{dn(z)}{dt} &= \frac{I}{edLW} - R(n(z)) \\ &\quad - \frac{\Gamma}{dW} \left\{ \sum_{k=1}^{N_s} g_m(\nu_k, n(z)) (N_{s_k}^+(z) + N_{s_k}^-(z)) \right\} \\ &\quad - \frac{2\Gamma}{dW} \left\{ \sum_{j=0}^{N_m-1} g_m(\nu_j, n(z)) K_j ((N_j^+(z) + N_j^-(z))) \right\} \end{aligned} \quad (48)$$

where  $I$  is the amplifier bias current. In (48) all of the bias current is assumed to pass through the active region only and not the surrounding InP regions. The bias current is assumed to have a uniform distribution across the active region width. The first term on the right hand side (RHS) of (48) represents the addition of carriers to the active region from the bias current. These injected carriers are then depleted by various mechanisms occurring within the amplifier. The recombination rate term  $R(n)$  is given by

$$R(n) = R_{\text{rad}}(n) + R_{\text{nr}}(n). \quad (49)$$

$R_{\text{rad}}(n)$  and  $R_{\text{nr}}(n)$  are the radiative and nonradiative carrier recombination rates, respectively, both of which can be expressed as polynomial functions of  $n$  [13], [14]

$$R_{\text{rad}}(n) = A_{\text{rad}}n + B_{\text{rad}}n^2 \quad (50)$$

$$R_{\text{nr}}(n) = A_{\text{nr}}n + B_{\text{nr}}n^2 + C_{\text{aug}}n^3 + D_{\text{leak}}n^{5.5}. \quad (51)$$

In (50),  $A_{\text{rad}}$  and  $B_{\text{rad}}$  are the linear and bimolecular radiative recombination coefficients. In (51),  $A_{\text{nr}}$  is a linear non-radiative recombination coefficient due to traps in the semiconductor material [14].  $B_{\text{nr}}$  represents nonradiative bimolecular recombination.  $C_{\text{aug}}$  is the Auger recombination coefficient and  $D_{\text{leak}}$  represents recombination due to leakage effects. Auger recombination and leakage effects can be significant in SOAs with high carrier densities. For the particular device considered, it is assumed that carrier leakage from the active region into surrounding InP regions is negligible [15].

The third and fourth terms on the RHS of (48) represent radiative recombination of carriers due to the amplified signal and amplified spontaneous emission (ASE).  $\Gamma$  is included as only this fraction of amplified photons resides in the active region. The factor of two in (48) accounts for the fact that spontaneously emitted photons can exist in one of two mutually orthogonal polarizations (TE or TM). In the model, the SOA is assumed to be polarization independent. Polarization dependence can be included by the use of different TE and TM optical confinement factors.

## VI. STEADY-STATE NUMERICAL ALGORITHM

As the SOA model equations cannot be solved analytically, a numerical solution is required. In the numerical model the amplifier is split into a number of sections labeled from  $i = 1$  to  $N_z$  as shown in Fig. 3. The signal fields and spontaneous emission photon rates are estimated at the section interfaces. In evaluating the RHS of (48),  $Q(i)$  for the  $i$ -th section, the signal and noise

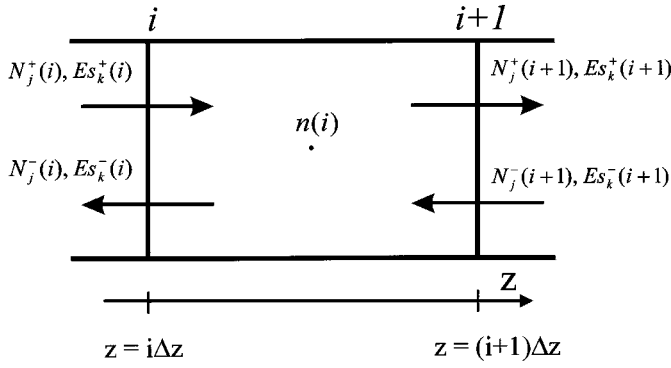


Fig. 3. The  $i$ th section of the SOA model. Signal fields and spontaneous emission are estimated at the section boundaries. The carrier density is estimated at the center of the section.

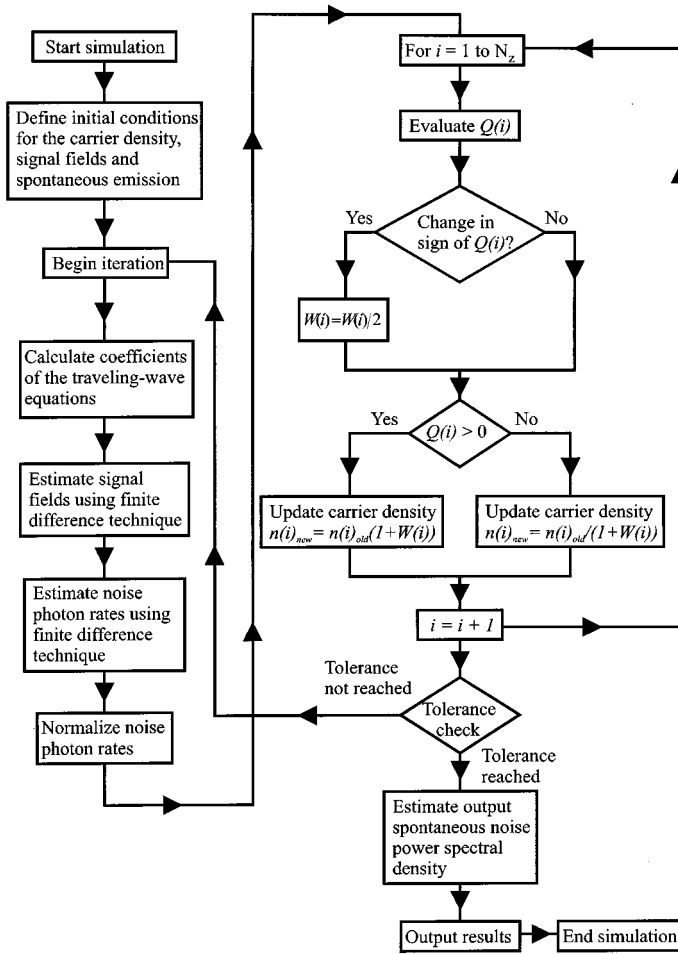


Fig. 4. SOA steady-state model algorithm. The algorithm updates the carrier density  $n(i)_{\text{new}}$  throughout the amplifier cavity so  $Q(i)$  [the RHS of (48)] approaches zero.

photon rates used are given by the mean value of those quantities at the section boundaries. In the steady-state  $Q(i)$  is zero. To predict the steady-state characteristics, an algorithm is used which adjusts the carrier density so the value of  $Q(i)$  throughout the amplifier approaches zero. A flowchart of the algorithm is shown in Fig. 4. The first step in the algorithm is to initialize the signal fields and spontaneous emission photon rates to zero. The initial carrier density is obtained from the solution of (48), with

all fields set to zero, using the Newton–Raphson technique [16]. The iteration now begins. The coefficients of the traveling-wave equations are computed. In the gain coefficient calculations, the radiative carrier recombination lifetime is approximated by

$$\tau = n/R_{\text{rad}}(n) = A_{\text{rad}} + B_{\text{rad}}n. \quad (52)$$

Next, the signal fields and noise photon densities are estimated using finite difference solutions of (20)–(21) and (34)–(35). Forward differences are used for positive traveling-waves and backward differences for negative traveling-waves. If  $X^+$  is a forward traveling-wave, then for the  $i$ th section, the spatial derivative is approximated by

$$\frac{dX^+}{dz} = \frac{X_i - X_{i-1}}{\Delta z}. \quad (53)$$

Similarly, if  $X^-$  is a backward traveling-wave, then for the  $i$ th section, the spatial derivative is approximated by

$$\frac{dX^-}{dz} = \frac{X_{i+1} - X_i}{\Delta z} \quad (54)$$

where  $\Delta z = L/N_z$  is the length of a single section. The noise normalization factors are then computed using trapezoidal integration of (46).  $Q(i)$  is then calculated for each section. If  $Q(i)$  is positive, then the carrier density is too low, in which case the new value of carrier density for the section is increased by a factor  $1 + W(i)$ .  $W(i)$  is a weight less than unity. An initial value for  $W(i)$  of 0.1 was found to give good convergence. If  $Q(i)$  is negative, then the carrier density is too high, in which case the new value of carrier density for the section is decreased by a factor  $1 + W(i)$ . If the sign of  $Q(i)$  differs from the previous iteration,  $W(i)$  is halved. This process enables convergence toward the correct value of carrier density by using smaller carrier density increments. The iteration continues until the percentage change in the signal fields, noise photon rates and carrier density throughout the SOA between successive iterations is less than the desired tolerance. When the iteration stops, the output spontaneous emission power spectral density is computed using the method of Section VII and parameters such as signal gain, noise figure and output spontaneous noise power are calculated. The algorithm shows good convergence and stability over a wide range of operating conditions.

## VII. ESTIMATION OF THE OUTPUT SPONTANEOUS EMISSION POWER SPECTRAL DENSITY

The average output noise photon rate spectral density (photons/s/Hz) after the coupling loss over both polarizations and bandwidth  $K_m \Delta \nu_m$  centered on  $\nu_j$  is

$$\sigma_N(\nu_j) = 2\eta_{\text{out}}(1 - R_2)K_j N_j^+(L)/(K_m \Delta \nu_m), \quad j = 0 \dots N_m - 1. \quad (55)$$

The average output noise photon rate spectral density  $\sigma_N(\nu_{\text{res},j})$  centered on the cavity resonance frequencies  $\nu_{\text{res},j}$  is interpolated using a cubic spline fit to the set of  $\sigma_N(\nu_j)$  points [16]. The amplifier resonant frequencies are given by

$$\nu_{\text{res},j} = \nu_c + \Delta \nu_c + j \Delta \nu_m, \quad j = 0 \dots K_m(N_m - 1). \quad (56)$$

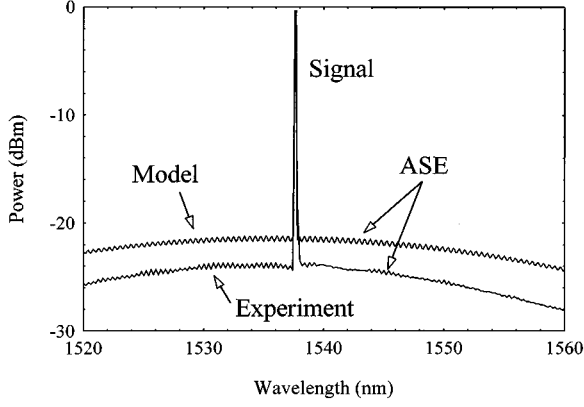


Fig. 5. SOA output spectrum. Resolution bandwidth is 0.1 nm. The input signal has a wavelength of 1537.7 nm and power of -25.6 dBm. Bias current is 130 mA. The predicted and experimental fiber-to-fiber signal gains are both 25.0 dB. The experimental gain ripple of 0.5 dB is identical to that predicted. The difference between the predicted and experimental ASE level is approximately 2.5 dB.

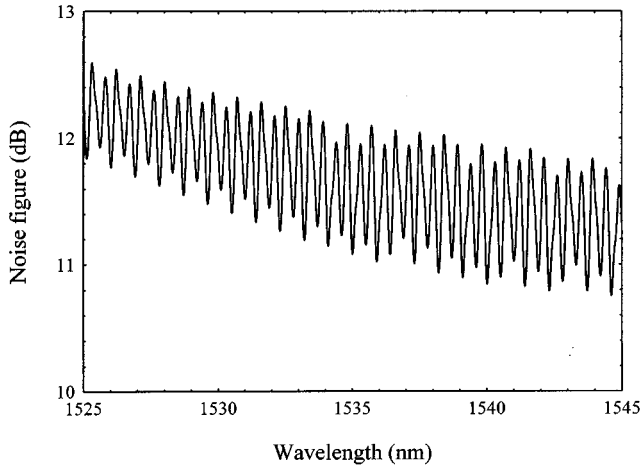


Fig. 6. Predicted SOA noise figure spectrum. Input parameters are as for Fig. 5. A noise figure of  $11.4 \pm 0.5$  dB at 1537.7 nm is predicted compared to an experimental value of  $8.8 \pm 0.3$  dB.

The anti-resonant frequencies are given by

$$\nu_{\text{ares},j} = \nu_{\text{res},j} - \Delta\nu_m/2, \quad j = 1 \dots K_m(N_m - 1). \quad (57)$$

The SOA gains at the resonant and anti-resonant frequencies are

$$G_{\text{res}}(\nu_{\text{res},j}) = \frac{(1 - R_1)(1 - R_2)G_s(\nu_{\text{res},j})}{(1 - \sqrt{R_1 R_2} G_s(\nu_{\text{res},j}))^2} \quad (58)$$

$$G_{\text{ares}}(\nu_{\text{ares},j}) = \frac{(1 - R_1)(1 - R_2)G_s(\nu_{\text{ares},j})}{(1 + \sqrt{R_1 R_2} G_s(\nu_{\text{ares},j}))^2} \quad (59)$$

where the single-pass gain at optical frequency  $\nu$  is given by

$$G_s(\nu) = \exp \left\{ \int_0^L [\Gamma g_m(\nu, n) - \alpha(n)] dz \right\}. \quad (60)$$

Trapezoidal integration is used to evaluate the integral in (60). The amplifier gain profile  $T(\nu)$  is obtained by fitting a cubic spline to the resonant and anti-resonant gain points. The output spontaneous emission noise power spectral density  $\sigma_{\text{ASE}}(\nu)$  (Watts/Hz) is determined by multiplying  $\sigma_N(\nu_{\text{res},j})$  by the

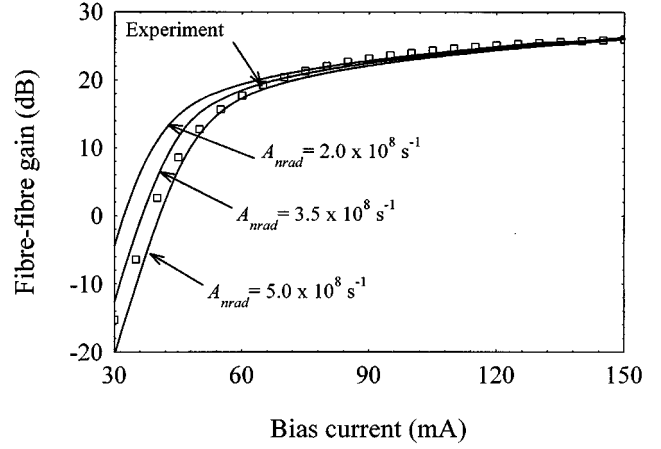


Fig. 7. Predicted and experimental SOA fiber-to-fiber gain versus bias current characteristics. The input signal has a wavelength of 1537.7 nm and power of -25.6 dBm. The device parameters are as in Table I, except for the nonradiative recombination coefficient  $A_{\text{rad}}$ .

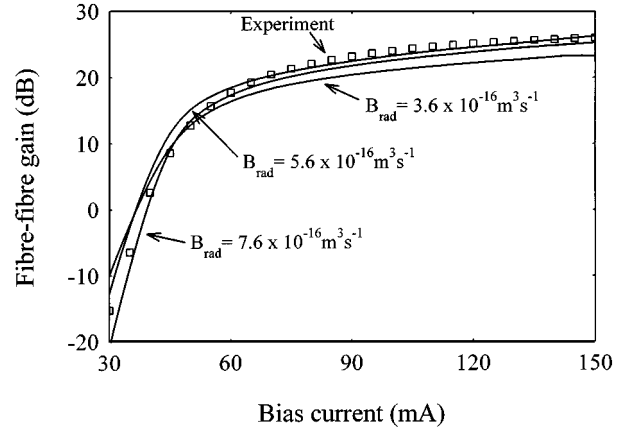


Fig. 8. Predicted and experimental SOA fiber-to-fiber gain versus bias current characteristics. The input signal has a wavelength of 1537.7 nm and power of -25.6 dBm. The device parameters are as in Table I, except for the nonradiative recombination coefficient  $B_{\text{rad}}$ .

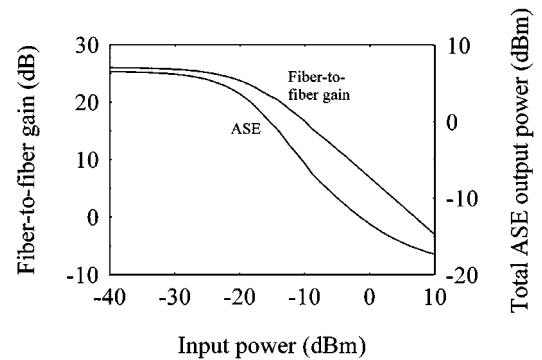


Fig. 9. SOA predicted fiber-to-fiber gain and output ASE power versus input signal power. Signal wavelength is 1537.7 nm and bias current is 130 mA.

photon energy  $h\nu$  and the ratio of the gain at that frequency  $T(\nu)$  to the average gain of the closest longitudinal mode  $j$  to  $\nu$ , i.e.,

$$\sigma_{\text{ASE}}(\nu) = \frac{h\nu \sigma_N(\nu_{\text{res},j}) T(\nu)}{\frac{1}{\Delta\nu_m} \int_{\nu_{\text{ares},j}}^{\nu_{\text{ares},j+1}} T(\nu') d\nu'}. \quad (61)$$

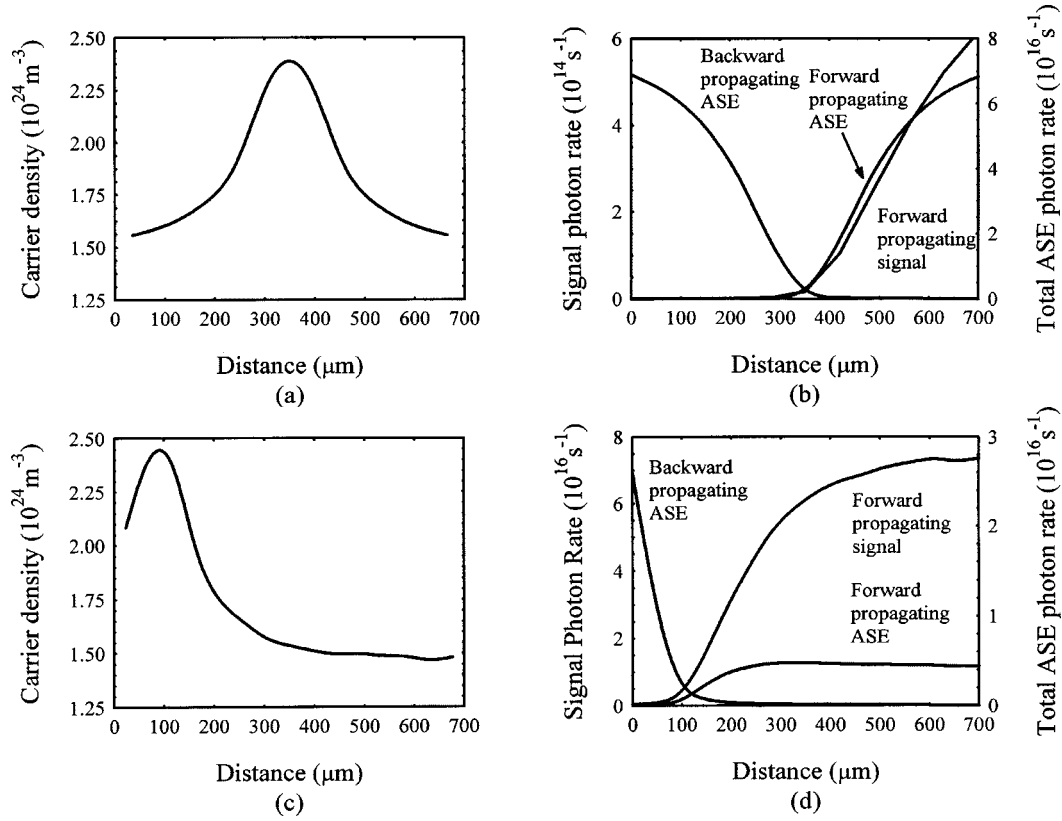


Fig. 10. SOA carrier density, forward- and backward-propagating total ASE photon rates and signal photon rates spatial distributions. Distance is measured from the SOA input facet. (a) and (b) -40 dBm input signal power. (c) and (d) -10 dBm input signal power. Saturation effects due to the amplified signal and ASE are evident. Signal wavelength is 1537.7 nm and the bias current is 130 mA.

The integral in the denominator of (61) is the average gain of the  $j$ -th longitudinal mode. From (61), the output spontaneous emission power into a frequency (resolution) bandwidth  $\Delta\nu$  centered on frequency  $\nu$  is

$$P_{\text{ASE}}(\nu) = \int_{\nu-\Delta\nu/2}^{\nu+\Delta\nu/2} \sigma_{\text{ASE}}(\nu') d\nu'. \quad (62)$$

This is the spontaneous emission power that would be displayed on an optical spectrum analyzer with a wavelength resolution bandwidth  $\Delta\lambda = c\Delta\nu/\nu^2$ .

### VIII. SIMULATIONS AND COMPARISON WITH EXPERIMENT

In Figs. 5–10, simulations are presented for the above SOA under a variety of operating conditions. The device temperature was 300 K. The loss and recombination coefficients used in the simulations were those that gave the best fit to the experimental gain versus bias current characteristic of Fig. 7. In the numerical simulations, the following settings were used:  $N_z = 10$ ,  $N_m = 40$ , and  $K_m = 20$ . In Fig. 5, the modeled and simulated SOA output spectra, at a bias current of 130 mA and input signal power of -25.6 dBm and signal wavelength of 1537.7 nm, are shown. The predicted gain ripple of 0.5 dB at the signal wavelength is identical to experiment. The predicted and experimental signal gain is 25.0 dB. The difference between the predicted and experimental ASE power levels is approximately 2.5 dB. This difference is probably because the amplifier length

used in the model is the mean amplifier length taking the tapers into account. This approximation has the effect of overestimating the noise relative to the amplified signal. However, the general shape of the predicted noise spectrum and gain ripple is close to experiment. Discrepancies between the simulation and experimental results are also caused by inaccuracies in estimation of the coupling losses, signal propagation, and loss and recombination coefficients. The signal propagation coefficient determines the positions of the ripple in the SOA gain spectrum. The exact location of the gain ripple is not an important operational parameter in SOA's with low facet reflectivities. In Fig. 6, the predicted noise figure spectrum is shown for an unsaturated SOA. The noise figure  $NF$  is calculated using the formula [17]

$$NF = 10 \log_{10} \left( \frac{\sigma_{\text{ASE}}(\nu)}{h\nu G(\nu)} + \frac{\eta_{\text{out}}}{G(\nu)} \right) \text{ (dB)} \quad (63)$$

where the amplifier input signal noise is assumed to be negligible.  $G(\nu)$  is the fiber-to-fiber gain at optical frequency  $\nu$ . A noise figure of  $11.4 \pm 0.5$  dB at 1537.7 nm is predicted compared with the experimental value of  $8.8 \pm 0.3$  dB. The difference here is due to the overestimation of the ASE noise by the model. In Fig. 7, predicted and experimental fiber-to-fiber gain versus bias current characteristics are shown. The shape of this characteristic depends largely on the values of the recombination coefficients used in (50)–(51). These coefficients are usually not known to a high degree of accuracy. The dependency on  $A_{\text{nrad}}$  is also shown in Fig. 7 for values of  $A_{\text{nrad}}$  of  $2.0 \times 10^8 \text{ s}^{-1}$  and  $5.0 \times 10^8 \text{ s}^{-1}$ . The dependence is more



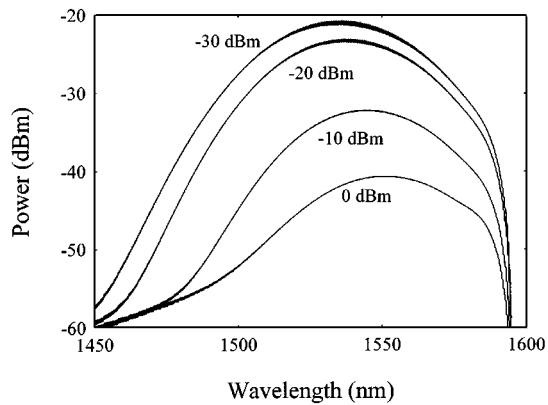


Fig. 11. Predicted SOA output ASE spectra with the input signal power as parameter, showing non-linear gain compression. Signal wavelength is 1537.7 nm and the bias current is 130 mA. Resolution bandwidth is 0.1 nm.

marked at lower bias currents, as the carrier density is lower and  $A_{\text{rad}}$  has greater influence on carrier recombination. Fig. 8 shows that the amplifier gain versus bias current characteristic is particularly sensitive to  $B_{\text{rad}}$ . This dependency is marked at all bias current levels. This is expected as the dominant radiative recombination mechanism is bimolecular. In Fig. 9, the predicted amplifier fiber-to-fiber gain and output ASE power versus input power characteristics are shown. These characteristics can be explained by reference to Fig. 10. In Fig. 10, the SOA carrier density, forward- and backward-propagating total ASE photon rates, and signal photon rates are shown as a function of distance for low and high input signal powers. The backward-propagating signal is negligible due to the low facet reflectivities. At low input powers, the carrier density has a symmetrical spatial distribution, peaking at the center of the SOA and tailing off toward the input and output facets as shown in Fig. 10(a). This is because the ASE peaks in these regions as shown in Fig. 10(b). At high input powers, the carrier density spatial distribution becomes more asymmetrical [Fig. 10(c)], with the peak moving toward the input facet. This is caused by the input signal dominating over ASE, as shown in Fig. 10(d). Analysis of spatial distributions can be used to aid SOA design. In Fig. 11, simulated SOA output ASE spectra are shown with the input signal power as parameter. The signal wavelength is near the unsaturated gain curve peak. At low signal power the carrier density is high giving a high signal gain. As the signal power is increased, the carrier density decreases causing the material gain spectrum peak to shift to longer wavelengths so reducing the signal gain even further. This is the well-known effect of nonlinear gain compression.

## IX. CONCLUSION

A wideband SOA steady-state model and numerical solution has been described. The model predictions show good agreement with experiment. The model can be used to investigate the effects of different material and geometrical parameters on SOA characteristics and predict wideband performance under a wide range of operating conditions.

## ACKNOWLEDGMENT

The author thanks N. J. Traynor and P. Maigne, Corning Fontainebleau Research Center, Avon, France for the use of experimental results and useful discussions.

## REFERENCES

- [1] L. Gillner, "Comparative study of some traveling-wave semiconductor laser amplifier models," in *Proc. Inst. Elect. Eng. J*, vol. 139, 1991, pp. 339–347.
- [2] D. A. Marcuse, "Computer model of an injection laser amplifier," *IEEE J. Quantum Electron.*, vol. QE-19, pp. 63–73, 1983.
- [3] R. Brosson, "Analytic model of a semiconductor optical amplifier," *J. Lightwave Technol.*, vol. 12, pp. 49–54, 1994.
- [4] A. J. Lowery, "Amplified spontaneous emission in semiconductor laser amplifiers: Validity of the transmission-line laser model," in *Proc. Inst. Elect. Eng. J*, vol. 137, 1990, pp. 241–247.
- [5] S. Ruiz-Moreno and J. Guitart, "Practical method for modeling the non-linear behavior of a traveling-wave semiconductor optical amplifier," *Proc. Inst. Elect. Eng. J*, vol. 140, pp. 39–43, 1993.
- [6] C. Deguet, D. Delprat, G. Crouzel, N. J. Traynor, P. Maigne, T. Pearsal, C. Lermiaux, N. Andreakis, C. Caneau, F. Favire, R. Bhat, and C. E. Zah, "Homogeneous buried ridge stripe semiconductor optical amplifier with near polarization independence," in *Proc. Eur. Conf. Optical Communications*, 1999.
- [7] A. Yariv, *Opt. Electron.*. New York: HWR International, 1985.
- [8] S. Adachi, *Physical Properties of III–IV Semiconductor Compounds*. New York: Wiley, 1992.
- [9] —, *GaAs and Related Materials*, Singapore: World Scientific, 1994.
- [10] N. G. Nilsson, "Empirical approximations for the Fermi energy of a semiconductor with parabolic bands," *Appl. Phys. Lett.*, vol. 33, pp. 653–654, 1978.
- [11] Y. Suematsu and A. R. Adams, *Handbook of Semiconductor Lasers and Photonic Integrated Circuits*, London, U.K.: Chapman & Hall, 1994.
- [12] M. J. Connelly and R. F. O'Dowd, "Travelling-wave semiconductor optical amplifier detector noise characteristics," in *Proc. Inst. Elect. Eng. J*, vol. 142, 1995, pp. 23–28.
- [13] R. Olshansky, C. A. Su, J. Manning, and W. Powazinik, "Measurement of radiative and nonradiative recombination rates in InGaAsP and AlGaAs light sources," *IEEE J. Quantum Electron.*, vol. QE-20, pp. 838–854, 1984.
- [14] M. Kot and K. Zdansky, "Measurement of radiative and nonradiative recombination rate in InGaAsP-InP LED's," *IEEE J. Quantum Electron.*, vol. 28, pp. 1746–1750, 1992.
- [15] M.-C. Amann and W. Thulke, "Current confinement and leakage currents in planar buried-ridge-structure laser diodes on *n*-substrate," *IEEE J. Quantum Electron.*, vol. 25, pp. 1595–1602, 1989.
- [16] W. H. Press, B. P. Flannery, S. A. Teukolsky, and W. T. Vetterling, *Numerical Recipes in Pascal*. Cambridge, MA: Cambridge Univ. Press, 1994.
- [17] J. C. Simon, P. Doussiere, L. Pophillat, and B. Fernier, "Gain and noise characteristics of a 1.5  $\mu\text{m}$  near-travelling-wave semiconductor laser amplifier," *Electron. Lett.*, vol. 25, pp. 434–436, 1989.
- [18] S. L. Chuang, *Physics of Optoelectronic Devices*. New York: Wiley Interscience, 1995.
- [19] B. R. Bennett, R. A. Soref, and J. A. Del Alamo, "Carrier-induced change in refractive index of InP, GaAs and InGaAsP," *IEEE J. Quantum Electron.*, vol. 26, pp. 113–122, 1990.

**Michael Connelly** (S'89–M'92) was born in Limerick, Ireland, in 1965. He received the B.E. and Ph.D. degrees in electronic engineering from the National University of Ireland, Dublin, in 1987 and 1992, respectively.

Since 1995, he has been a Lecturer in Electronic Engineering at the University of Limerick. His current research interests are SOA gate arrays, fiber cavity sensors, and optical metrology.

# Comments and Corrections

## Corrections to “Wideband Semiconductor Optical Amplifier Steady-State Numerical Model”

Michael J. Connelly

In Table I of the above paper,<sup>1</sup> the correct value of  $K_1$  is  $7500 \times 10^{-24} \text{ m}^2$ .

Equation (35) should be

$$\frac{dN_j^-(z)}{dz} = (\Gamma g_m(v_j, n) - \alpha(n))N_j^- R_{sp}(v_j, n). \quad (35)$$

The integral in equation (46) can also be written as

$$\frac{1}{\pi} \int_0^\pi \frac{d\phi}{1 + \gamma^2 \sin^2 \phi} = \frac{1}{\sqrt{1 + \gamma^2}}. \quad (46)$$

Equation (52) should be

$$\tau = n / R_{\text{rad}}(n) = (A_{\text{rad}} + B_{\text{rad}} n)^{-1}. \quad (52)$$

Manuscript received June 25, 2001.

The author is with the Department of Electronic and Computer Engineering, University of Limerick, Limerick, Ireland (e-mail: michael.connelly@ul.ie).  
Publisher Item Identifier S 0018-9197(01)07829-0.

<sup>1</sup>IEEE J. Quantum Electron., vol. 37, pp. 439–447, Mar. 2001.

## Corrections to “Electrooptic Effects in GaAs–AlGaAs Narrow Coupled Quantum Wells”

M. P. Earnshaw and D. W. E. Allsopp

In the above paper,<sup>1</sup> Table I was erroneously repeated in place of Table II. The correct Table II is shown here.

Structure	$s_{TE}$ $\times 10^{-19}$ $\text{m}^2/\text{V}^2$	$\Delta n_{QEO}$ $\times 10^{-4}$	$L_\pi$ mm	$L_\pi$ loss DB
Shallower SCQW	32	17.2	0.78	0.74
Deeper SCQW	18	9.6	1.34	2.23
6 nm SQW	13	7.0	2.00	0.68
7.5 nm $\text{Al}_{0.3}\text{Ga}_{0.7}\text{As}/\text{GaAs}$	8	4.3	3.47	~0.5

Manuscript received July 1, 2001.

M. P. Earnshaw was with the Department of Electronics, University of York, York, U.K. He is now with Bell Laboratories, Lucent Technologies, Murray Hill, NJ 07974 USA.

D. W. E. Allsopp is with the Department of Electronic and Electrical Engineering, University of Bath, Bath BA2 7AY, U.K.

Publisher Item Identifier S 0018-9197(01)07934-9.

<sup>1</sup>IEEE J. Quantum Electron., vol. 37, pp. 897–904, July 2001.